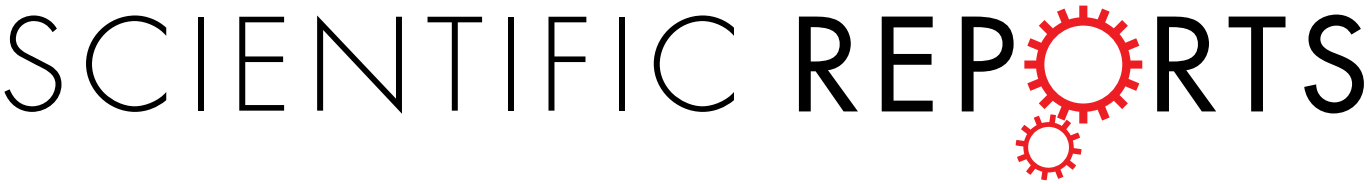

OPEN

Optical properties of monolayer tinene in electric fields

Rong-Bin Chen[1], Szu-Chao Chen[2], Chih-Wei Chiu[3] & Ming-Fa Lin[2]

Received: 19 January 2017
Accepted: 31 March 2017
Published online: 12 May 2017

The absorption spectra of monolayer tinene in perpendicular electric fields are studied by the tight-binding model. There are three kinds of special structures, namely shoulders, logarithmical symmetric peaks and asymmetric peaks in the square-root form, corresponding to the optical excitations of the extreme points, saddle points and constant-energy loops. With the increasing field strength, two splitting shoulder structures, which are dominated by the parabolic bands of $5p_z$ orbitals, come to exist because of the spin-split energy bands. The frequency of threshold shoulder declines to zero and then linearly grows. The third shoulder at 0.75~0.85 eV mainly comes from ($5p_x$, $5p_y$) orbitals. The former and the latter orbitals, respectively, create the saddle-point symmetric peaks near the M point, while they hybridize with one another to generate the loop-related asymmetric peaks. Tinene quite differs from graphene, silicene, and germanene. The special relationship among the multi-orbital chemical bondings, spin-orbital couplings and Coulomb potentials accounts for the feature-rich optical properties.

The layered condensed-matter systems, with the nano-scaled thickness, have attracted a lot of theoretical[1–5] and experimental[6–12] researches, mainly owing to the unusual geometric symmetry and the rich intrinsic interactions. Specifically, the 2D group-IV systems have the hexagonal symmetry, the unique orbital hybridizations, and the significant spin-orbital couplings (SOCs). They are the ideal 2D materials for studying the diverse physical, chemical and material phenomena[1–3, 13, 14] and are expected to have high potentials in the near-future technological applications[10, 15–17]. Graphene could be produced by various experimental methods[8, 9, 18–22] since the first discovery in 2004. Silicene and germanene have been fabricated on metallic substrates[10, 11, 23–26]. Recently, tinene is successfully synthesized on a substrate of bismuth telluride[12]. In addition, monolayer Pb system is absent in the experimental growth up to now. Graphene has a very strong sp^2 bonding on a planar structure, while silicene, germanene and tinene possess the buckled structure with a mixed sp^2-sp^3 hybridization. The spin-orbital coupling is almost negligible in the former, but very important for the latter. Among three buckled systems, tinene exhibits the strongest sp^3 bonding and SOC. These two critical interactions can dramatically change the electronic energy spectra[27] and thus create the rich optical properties[28, 29]. For monolayer tinene, absorption spectra, which arise from the cooperation of the orbital- and spin-dependent interactions and the external electric field ($\mathbf{F} = F\hat{z}$), will be explored in detail. A comparison with other group-IV systems is also made.

It is well known that the low-energy essential properties of monolayer graphene are dominated the $2p_z$-orbital hybridization and the hexagonal honeycomb symmetry. This system is a zero-gap semiconductor, with a vanishing density of states (DOS) at the Fermi level ($E_F = 0$), since there exists an isotropic Dirac cone formed by the linearly intersecting valence and conduction bands. Silicene and germanene possess the significant SOCs much stronger than that in graphene. Such SOCs can separate the Dirac-cone structures built from the dominating $3p_z$ or $4p_z$ orbitals, so that the intrinsic systems are direct-gap semiconductors with $E_g \sim 5$ and 45 meVs for Si & Ge, respectively[3, 30]. As to tinene, the theoretical calculations predict that the low-lying energy bands arising from the ($5p_x$, $5p_y$, $5p_z$) orbitals appear simultaneously, directly reflecting the tight cooperation between the serious sp^3 hybridizations and the strong SOCs[31, 32]. A small indirect gap of $E_g \sim 54$ meV is mainly determined by the separated Dirac-cone structure and the ($5p_x$, $5p_y$)-dominated energy bands. Moreover, an external electric field can be applied to modulate the essential properties of the buckled systems, such as, the obvious changes in band gap, energy dispersions and state degeneracy[5, 33].

In this work, the tight-binding model[34, 35] and the gradient approximation[36, 37] are, respectively, utilized to evaluate electronic and optical properties of monolayer tinene. The sp^3 chemical bonding, SOCs and electric

[1]Center of General Studies, National Kaohsiung Marine University, Kaohsiung, 811, Taiwan. [2]Department of Physics, National Cheng Kung University, Tainan, 701, Taiwan. [3]Department of Physics, National Kaohsiung Normal University, Kaohsiung, 824, Taiwan. Correspondence and requests for materials should be addressed to R.-B.C. (email: rbchen@mail.nkmu.edu.tw) or M.-F.L. (email: mflin@mail.ncku.edu.tw)

field are included in the calculations. The orbital- and F_z-dependent absorption spectra are thoroughly investigated. This study shows that the feature-rich electronic structures are responsible for the diverse optical spectra. There are three kinds of critical points in the energy-wave-vector space, including the extreme and the critical points, and the constant-energy loops centered at certain extreme points. They, respectively, lead to the shoulder structure, the logarithmic-form symmetric peaks and the square-root asymmetric peaks in absorption spectra. Furthermore, the threshold frequency and the initial structures are easily tuned by an electric field. Tinene sharply contrasts with graphene, silicene and germanene in the main features of optical properties, e.g., the form, number, frequency and intensity of the low- and middle-frequency absorption structures. The predicted results could be verified by the optical spectroscopy[38].

Methods

Monolayer tinene has a buckled structure, in which the A & B equivalent sublattices are located at two parallel planes with a separation of $2l$ ($l = 0.42$ Å; Fig. 1(a)). The lattice constant in the same sublattice is 4.7 Å, and the angle between the Sn-Sn bond and the z-axis is 107.1°. There are two Sn atoms in a primitive unit cell. Each atom contributes ($5s$, $5p_x$, $5p_y$, $5p_z$) orbitals to electronic structures; furthermore, the spin-up and spin-down configurations dominate the on-site SOCs. The Hamiltonian built from the orbital- and spin-dependent tight-binding function is a 16×16 Hermitian matrix. In the presence of a uniform perpendicular electric field, the tight-binding Hamiltonian, with the nearest-neighbor interactions, is expressed as

$$\begin{aligned} H &= \sum_{\langle i\rangle,o,s} E_o C^+_{ios} C_{ios} + \sum_{\langle i,j\rangle,o,o',s} \gamma^{\vec{R}_{ij}}_{oo'} C^+_{ios} C_{jo's} + \sum_{\langle i\rangle,p_\alpha,p_\beta,s,s'} \frac{\lambda_{soc}}{2} C^+_{ip_\alpha s} C_{ip_\beta s'} (-i\varepsilon_{\alpha\beta\gamma}\sigma^\gamma_{ss'}) \\ &\quad + l \sum_{\langle i\rangle,o,s} \mu_i F C^+_{ios} C_{ios}, \end{aligned} \tag{1}$$

where $i(j)$, $o(o')$, and $s(s')$ represent the lattice site, atomic orbital, and spin, respectively. The site energy of $5s$ orbital is -6.23 eV, as measured from that of the $5p$ orbitals. E_o and $\gamma^{\vec{R}_{ij}}_{oo'}$ are site energy and hopping integral, respectively. The latter depends on the type of atomic orbitals with the nearest-neighbor vector $\vec{R}_{ij}$, in which the Slater-Koster hopping interactions are $V_{ss\sigma} = -2.6245$ eV, $V_{sp\sigma} = 2.6504$ eV, $V_{pp\sigma} = 1.4926$ eV, and $V_{pp\pi} = -0.7877$ eV[30,39]. The third term of $\lambda_{soc} = 0.8$ eV is, the effective SOC on the same atom. α, β, and γ denote the x, y, and z components, and σ is the Pauli matrix. The last term is the F-induced Coulomb potential energy with $\mu_i = +1(-1)$ for the A(B) site.

When monolayer tinene exists in an electromagnetic field, electrons are excited from the occupied states to the unoccupied ones under the vertical transitions. The initial and final states have the same wave vector ($\Delta k_x = 0$, $\Delta k_y = 0$) as a result of the almost vanishing photon momentum. Based on the Fermi's golden rule, the optical absorption is given by

$$\begin{aligned} A(\omega) \;\propto\; & \sum_{h,h',n,n'} \int_{1^{st}BZ} \frac{dk_x dk_y}{(2\pi)^2} \left| \left\langle \Psi^{h'}_{n'}(k_x, k_y) \middle| \frac{\widehat{E}\cdot\mathbf{P}}{m_e} \middle| \Psi^{h}_{n}(k_x, k_y) \right\rangle \right|^2 \\ & \times Im\left[\frac{f(E^{h'}_{n'}(k_x, k_y)) - f(E^{h}_{n}(k_x, k_y))}{E^{h'}_{n'}(k_x, k_y) - E^{h}_{n}(k_x, k_y) - (\omega + i\gamma)} \right], \end{aligned} \tag{2}$$

where $f(E^h_n(k_x, k_y))$ is the Fermi-Dirac distribution function, $\widehat{E}$ the unit vector of an electric polarization, and γ ($=10$ meV) the broadening parameter. Energy band ($E^h_n(k_x, k_y)$) and wave function ($\Psi^h_n(k_x, k_y)$) are obtained from diagonalizing the Hamiltonian in Eq. (1). h represents the valence or conduction band, and n corresponds to the nth band measured from the Fermi level. An electric polarization of $\widehat{E} \| \hat{x}$ is chosen for a model study at zero temperature, since the direction-dependence of absorption spectrum is negligible. The velocity matrix element in Eq. (2) is approximated by the gradient of Hamiltonian versus k_x. Similar approximations have been successfully applied to comprehend optical spectra of carbon nanotubes[37] and few-layer graphenes[36].

Results and Discussion

Monolayer tinene exhibits three pairs of valence and conduction bands in the range of $-3\,\text{eV} \le E^{c,v} \le 3\,\text{eV}$, as clearly shown in Fig. 1(b). They are mainly determined by the ($5p_x$, $5p_y$, $5p_z$) orbitals (Fig. 1(c)); therefore, the $5s$ orbitals make important contributions only at deeper or higher energies. Each band is doubly degenerate in the spin degree of freedom; that is, the up- and down-dominated electronic states are degenerate to each other. The low-lying energy bands near the K/K′ and Γ points appear simultaneously. Without the SOC, the isotropic Dirac-cone structure due to the $5p_z$ orbitals is gapless at the corners of the first Brillouin zone (black curve in Fig. 1(b)). The first and second pairs of energy bands near the Γ point, with double degeneracy, mainly come from the ($5p_x$, $5p_y$) orbitals. Specifically, the SOC creates the slightly deformed Dirac cones with an energy spacing of ~0.12 eV and the splitting/anti-crossing of the first and second valence (conduction) bands (green curves). The lowest unoccupied state and the highest occupied state are, respectively, situated at the K/K′ and Γ points, i.e., there exists an indirect gap of ~54 meV. Electronic structures have three kinds of energy bands, namely, linear, parabolic and partial flat energy dispersions (centered at the K or Γ point). Apparently they reveal the critical points in the energy-wave-vector space (Fig. 2). The extreme (minima & maxima) and saddle points, respectively, correspond to the (K/K′, Γ) and M ones (triangles and squares in Fig. 1(b); some of them in Fig. 2(a–c)). It is also noticed that the unusual constant-energy loops occur in between the Γ and M (K/K′) points (circles in Fig. 1(b)).

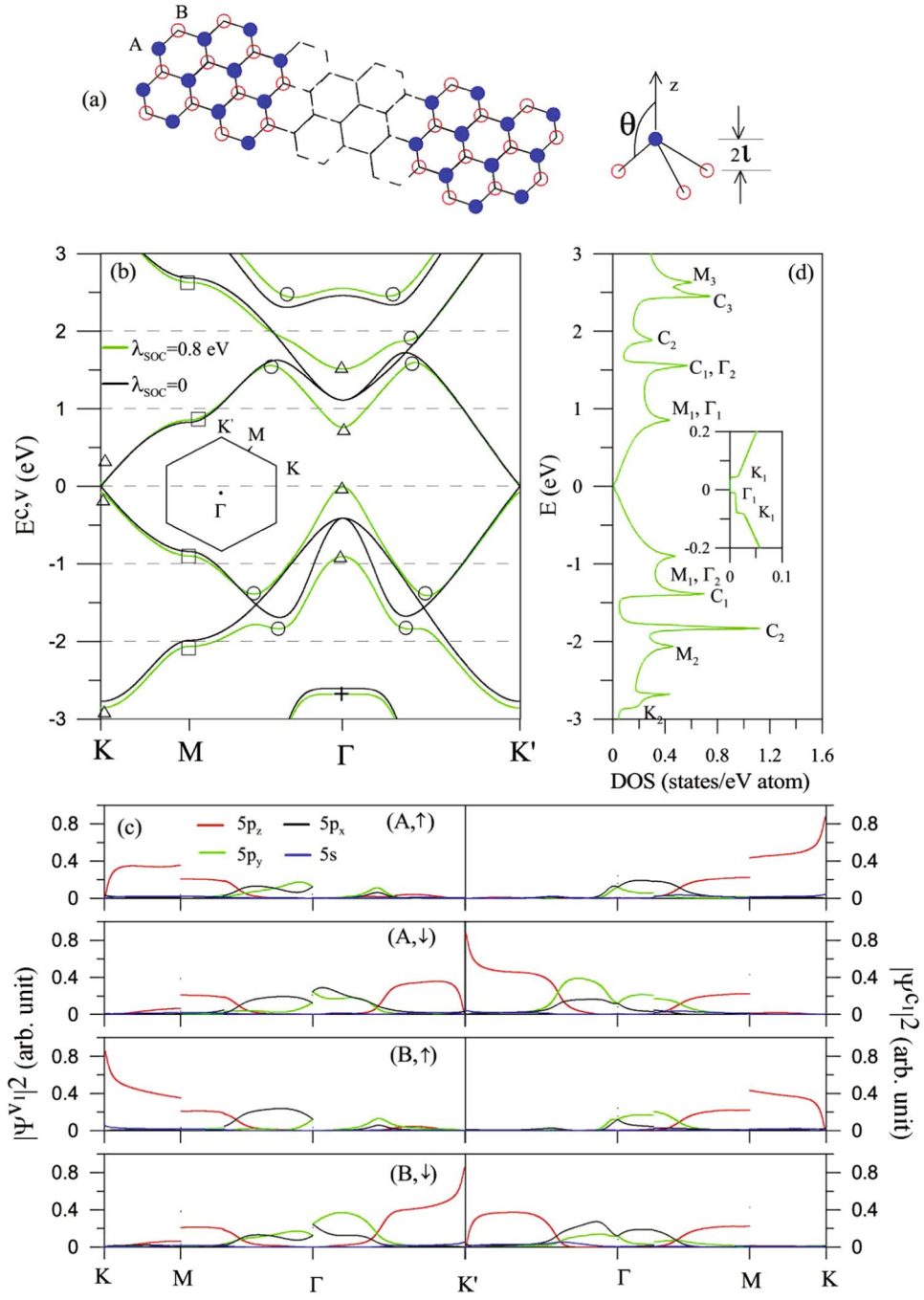

Figure 1. For monolayer tinene: (**a**) *xy*-plane geometric structure & sp^3 bonding, (**b**) three pairs of energy bands along the high symmetry points & the first Brillouin zone, (**c**) orbital-dependent wave-function probabilities for the first pair of energy bands; (**d**) density of states & the low-energy result in the inset. The subscripts in (**c**) are associated with the *n*-th energy band measured from the Fermi level.

Those of the first and second pairs of energy bands are due to the cooperation of the sp^3 bonding and SOC (black and green curves in Fig. 1(b)), e.g., that of the first valence band in Fig. 2(b). The feature-rich energy dispersions and critical points will dominate the special structures in DOSs and absorption spectra. They could be directly examined by the angle-resolved photo-emission spectroscopy (ARPES)[40–43].

DOS of monolayer tinene, defined as

$$D(E) = \sum_{n,h=c,v} \int_{1^{st}BZ} \frac{dk_x dk_y}{(2\pi)^2} \frac{\gamma}{\pi} \frac{1}{[E - E_n^h(k_x, k_y]^2 + \gamma^2}, \tag{3}$$

presents a lot of special structures in Fig. 1(d). The shoulder structures (triangles), the logarithmic-form symmetric peaks (squares), the square-root peaks (circles) and the delta-function-like peaks (crosses), respectively,

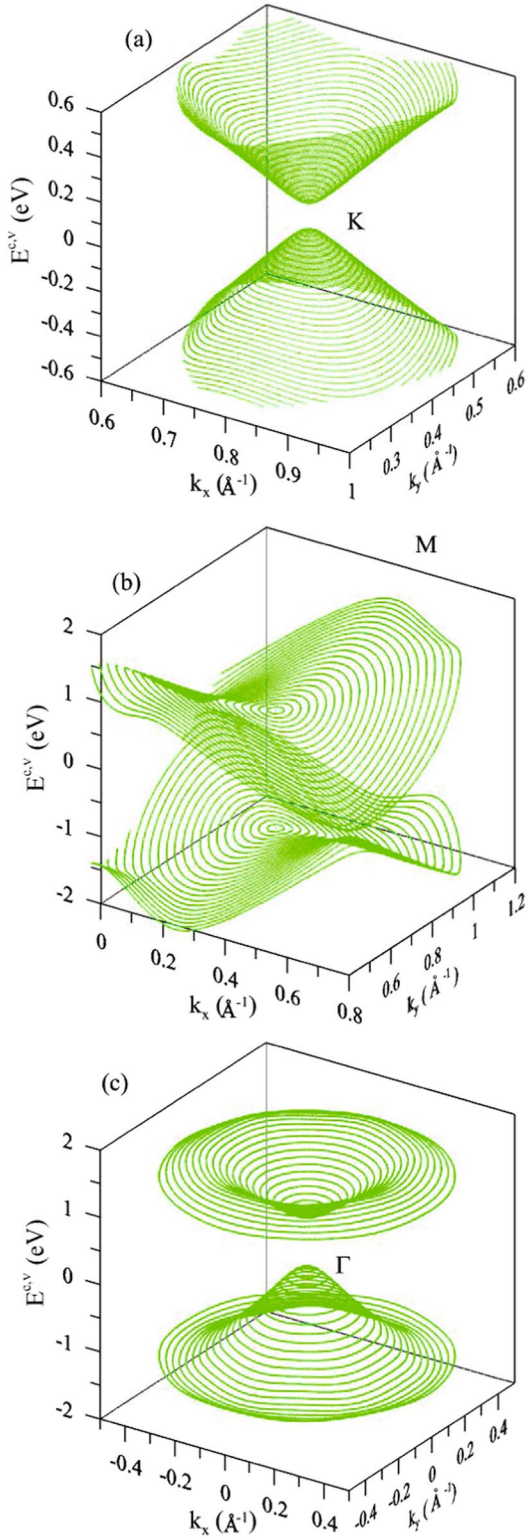

Figure 2. The low-lying electronic structures in the energy-wave-vector space near the (**a**) K, (**b**) M and (**c**) Γ points.

originate from the extreme points, the saddle points, the constant-energy loops with infinite extreme points (regarded as the 1D parabolic bands), and the partially flat energy dispersions. The first and second (third) structures might be merged together due to the close energies. The above-mentioned special structures could be further divided into the orbital-created ones. The $5p_z$-dependent features cover a pair of shoulder structures centered at $E = 0$ (K in the inset), two symmetric peaks at $E = \pm 0.9$ eV, and a symmetric peak at $E = -2.7$ eV. The ($5p_x$, $5p_y$, $5p_z$) orbitals co-dominate all the asymmetric peaks. The other shoulder structures and symmetric peaks are

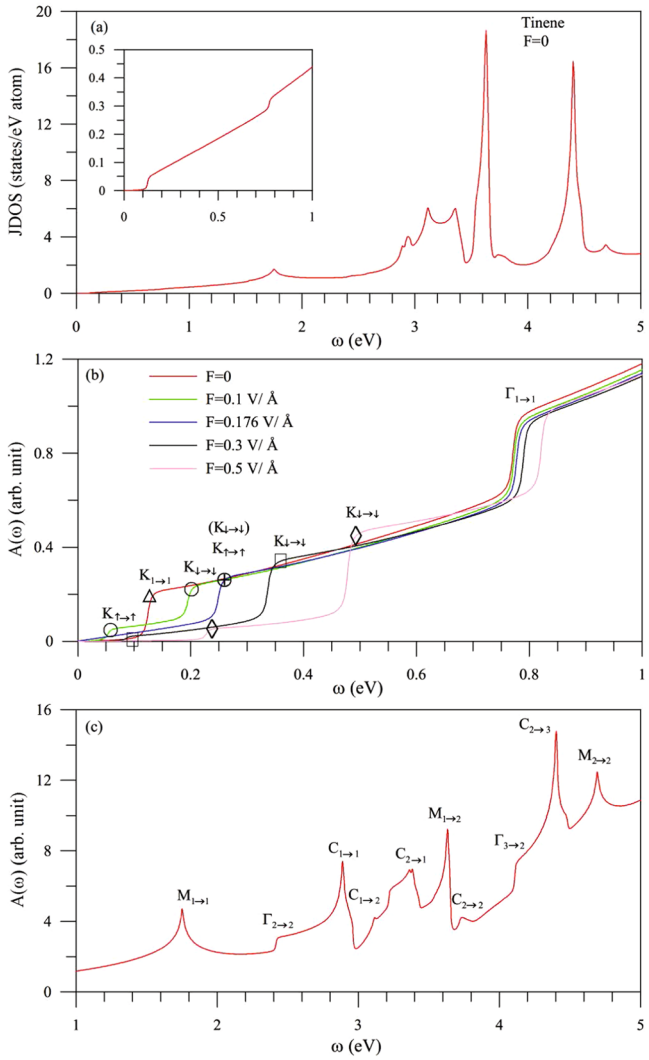

Figure 3. Optical properties of tinene: (**a**) joint density of states; the (**b**) low- and (**c**) middle-frequency absorption spectra. Inset in (**a**) is the low-ω JDOS. Also shown in (**b**) is the F-induced spectra.

closely related to the ($5p_x$, $5p_y$) orbitals. The STS measurements, in which the tunneling conductance (dI/dV) is proportional to DOS, can serve as efficient methods to examine the special structures in DOS. They have been successfully utilized to verify the diverse electronic properties in few-layer graphenes[44–47], graphene nanoribbons[48, 49], and carbon nanotubes[50–52]. The experimental verifications on the rich structures could provide the useful information about the orbital- and SOC-dominated energy bands in tinene.

Absorption spectra strongly depend on joint density of states (JDOS) and the velocity matrix elements. The former represents all the available excitation channels under the vertical transitions. JDOS, as clearly indicated in Fig. 3(a), has a lot of special structures due to the initial and final critical points. $A(\omega)$, which directly reflects the main features of energy dispersions, exhibits two low-frequency shoulder structures at $\omega = 0.12$ & 0.75 eVs (red curve in Fig. 3(b)). The threshold shoulder originates from the excitation between two separated Dirac points (Fig. 1(b); $K_{1\to1}$) and the second one from the first pair of energy bands near the Γ point ($\Gamma_{1\to1}$). They are dominated by the $5p_z$ and ($5p_x$, $5p_y$) orbitals, respectively. Also, the first pair of valence and conduction bands can create a logarithmic-form peak and a square-root peak at $\omega = 1.75$ & 2.94 eVs (Fig. 3(c)), respectively, corresponding to the M saddle points and constant-energy loops ($M_{1\to1}$ and $C_{1\to1}$). The symmetric one associated with the $5p_z$ orbitals has absorption frequency about double that of $V_{pp\pi}$, as observed in graphene, silicene and germanene (Fig. 5 is discussed latter). The asymmetric one due to the ($5p_x$, $5p_y$, $5p_z$) orbitals is determined by the SOC and sp^3 bonding.

The spectral structures of optical excitations, which are closely related to the second and third pairs of energy bands, occur at the middle-frequency range of $2\,\text{eV} \le \omega \le 5\,\text{eV}$ (Fig. 3(c)). Part of them arise from the intra-pair optical excitations, including the extreme and saddle points ($\Gamma_{2\to2}$ and $M_{2\to2}$); the constant-energy loops in the second pair ($C_{2\to2}$). There exist the significant inter-pair optical excitations, such as the structures due to $\Gamma_{3\to2}$, $M_{1\to2}$, $C_{1\to2}$, $C_{2\to1}$, and $C_{2\to3}$. In addition, few structures associated with the deeper- or higher-energy bands are

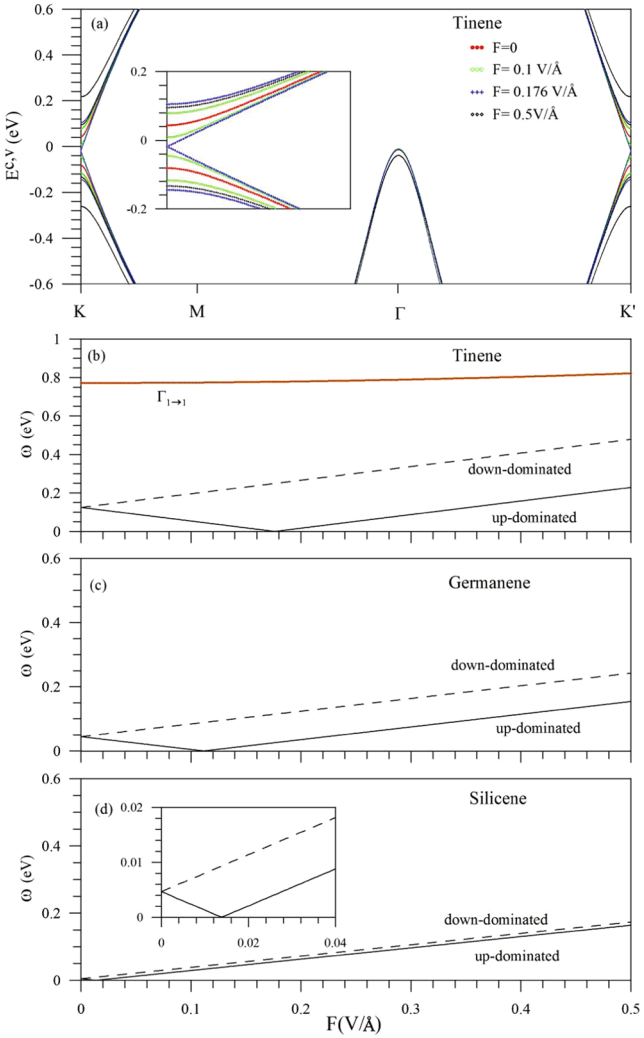

Figure 4. (**a**) Energy bands of tinene in the range of $-0.6\,\text{eV} \leq E^{c,v} \leq 0.6\,\text{eV}$ at various electric fields, and (**b**) the F-dependent absorption frequencies within $\omega \leq 1\,\text{eV}$ for (**b**) tinene, (**c**) germanene and (**d**) silicene.

not assigned the specific excitation channels. The feature-rich absorption spectra clearly illustrate the strong cooperation between the sp^3 bonding and SOC.

The electric field can dramatically change band structure and thus absorption spectrum, especially for the low-energy essential properties. F destroys the mirror symmetry about the $z = 0$ plane, leading to the spin-split energy bands (Fig. 4(a)). With the gradual increase of F, the spin up-dominated valence and conduction bands near the Dirac points approach to E_F (solid curves). Energy gap is vanishing at the critical field $F_c = 0.176\,\text{V/Å}$, in which the linear Dirac-cone structure is recovered. Moreover, E_g is opened under the further increase of F. However, the spin down-dominated energy bands deviate from E_F monotonously (dashed curves). As a result, the optical threshold shoulder becomes two splitting ones, as clearly indicated in Fig. 3(b) at various Fs. The absorption frequency of the first structure declines, reaches zero, and then grows in the increment of F (Fig. 4(b)). That of the second one increases smoothly. The similar results could be observed in germanene and silicene (Fig. 4(c,d)). On the other hand, energy bands near the Γ point remain double degeneracy and makes main contributions to the third shoulder with the monotonous F-dependence (the third absorption frequency in Fig. 4(b)). In short, the cooperation of the Coulomb potential and SOC results in the spin-split electronic states near the K and K′ valleys, but not the Γ valley.

Tinene is in sharp contrast to other group-IV systems in band structures and optical properties, as indicated from Figs 1, 3, 4 and 5. Germanene, silicene and graphene do not have the low-lying energy bands near the Γ point, so that they exhibit the direct or vanishing energy gaps (Fig. 5(a–c)) and the lower threshold absorption frequencies (Fig. 4(c,d)). The parabolic bands centered at the Γ point possess the deeper or higher state energies; therefore, the second shoulder structure cannot be observed in the range of $\omega < 1\,\text{eV}$. The constant-energy loop is absent in the first valence band, leading to the disappearance of asymmetric peaks in absorption spectra. The number of critical points within $|E^{c,v}| \leq 3\,\text{eV}$ is less than that of tinene, and so do the spectral structures. Among these four systems, graphene has the highest absorption frequency in the $M_{1\to1}$ excitations (the π-electronic excitations), owing to the strongest hopping interaction of the p_z orbitals ($V_{pp\pi}$). The strengths of

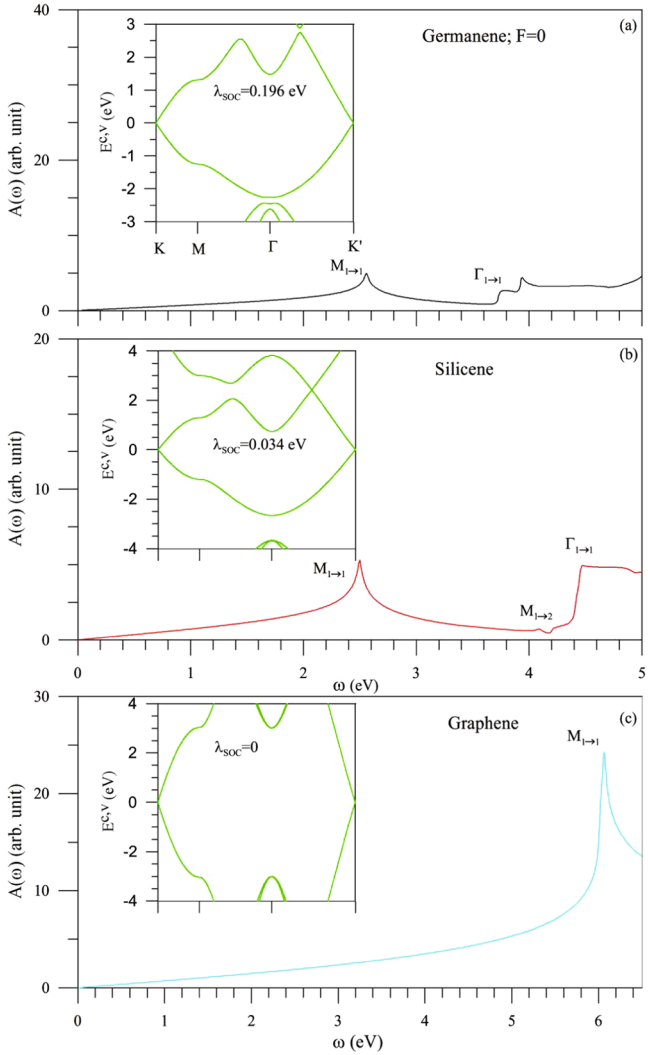

Figure 5. Band structures and absorption spectra for (**a**) germanene (**b**) silicene, and (**c**) graphene.

orbital hybridizations and SOC can account for the above-mentioned critical differences. On the other hand, tinene, germanene and silicene exhibit the narrow gaps and the *F*-dependent splitting effects on the low-energy essential properties.

Optical spectroscopies[53–57] have been utilized to identify the rich excitation properties in the low-dimensional carbon-related systems, such as, few-layer graphenes[53–57] and carbon nanotubes[58,59]. Such systems possess the ~5–6-eV strong π peak corresponding to the optical excitations of saddle points. This peak, which arises from the π bondings of p_z orbitals, is predicted to exist in other group-IV 2D systems (Figs 3 and 5). The AB- and ABC-stacked graphenes are different from each other in the absorption frequencies, spectral structures and *F*-induced excitation spectra[53–57]. Moreover, carbon nanotubes exhibit the strong dependence of asymmetric absorption peaks on radius and chirality[58,59]. The unique optical properties of tinene are worthy of detailed experimental examinations, including shoulders, symmetric peaks, asymmetric peaks, and *F*-dependent excitation frequencies and absorption structures. These directly reflect the unusual critical points and the coupling effect of sp^3 bondings and SOC. The optical experiments, accompanied with the ARPES and STS measurements, are very useful in fully understanding the critical orbital hybridizations and SOC and thus the important differences among group-IV 2D systems.

Conclusion

By the tight-binding model and gradient approximation, we have calculated for monolayer tinene the electronic structure, DOS and absorption spectrum. The close relationship among the sp^3 bonding, SOC and electric field is responsible for the diverse essential properties. Tinene quite differs from germanene, silicene and graphene in band structures and optical spectra, mainly owing to the strength of orbital hybridizations and SOC. The predicted results could be verified by ARPES, STS, and optical spectroscopy.

The main features of energy bands lie in the critical points and the orbital-, spin- and *F*-dependence. The form, the extreme and saddle points & the constant-energy loops, have the unusual DOS and spectral structures. They exhibit the shoulders, and the symmetric and asymmetric peaks in DOS, respectively. The K/K′ valleys and the

first pair of saddle points mainly come from the $5p_z$ orbitals. The ($5p_x$, $5p_y$, $5p_z$) co-dominate the constant-energy loops. The other critical points are closely related to the ($5p_x$, $5p_y$) orbitals. The spin up- and down-dominated energy bands in the deformed Dirac cones are split by an external electric field, leading to a non-monotonous dependence of E_g on F. All the critical points create a lot of special structures in absorption spectra under the vertical transitions of the intra- and inter-pair of energy bands. Specifically, the structures due to the first pair of energy bands cover the first and second shoulders, a symmetric peak and a asymmetric peak, corresponding to the (K, Γ, M) points and constant-energy loops, respectively. The Γ-induced low-frequency shoulder and the asymmetric peak are absent in other group-IV systems. The first shoulder becomes two splitting ones in the presence of F. Moreover, there exist many structures above the middle frequency, being associated with three pairs of energy bands. In addition, germanene and silicene exhibit the F-dependent splitting behavior, and all the systems have the prominent π-electronic absorption peaks. The experimental measurements on energy bands, DOS and optical spectra could identify the orbital hybridizations, the strength of SOC and the effects of electric field in 2D group-IV systems.

References

1. Zheng, Y. & Ando, T. Hall conductivity of a two-dimensional graphite system. *Phys. Rev. B* **65**, 245420, doi:10.1103/PhysRevB.65.245420 (2002).
2. Gusynin, V. P. & Sharapov, S. G. Unconventional integer quantum Hall effect in graphene. *Phys. Rev. Lett.* **95**, 146801, doi:10.1103/PhysRevLett.95.146801 (2005).
3. Liu, C. C., Feng, W. & Yao, Y. Quantum spin Hall effect in silicene and two-dimensional germanium. *Phys. Rev. Lett.* **107**, 076802, doi:10.1103/PhysRevLett.107.076802 (2011).
4. Xu, Y. *et al*. Large-gap quantum spin Hall insulators in tin films. *Phys. Rev. Lett.* **111**, 136804, doi:10.1103/PhysRevLett.111.136804 (2013).
5. Ezawa, M. Valley-polarized metals and quantum anomalous Hall effect in silicene. *Phys. Rev. Lett.* **109**, 055502, doi:10.1103/PhysRevLett.109.055502 (2012).
6. Radisavljevic, B., Radenovic, A., Brivio, J., Giacometti, V. & Kis, A. Single-layer MoS_2 transistors. *Nat. Nanotech.* **6**, 147–50, doi:10.1038/nnano.2010.279 (2011).
7. Hao, K. *et al*. Direct Measurement of Exciton Valley Coherence in Monolayer Wse_2. *Nat. Phys.* **12**, 677–682, doi:10.1038/nphys3674 (2016).
8. Novoselov, K. S. *et al*. Electric field effect in atomically thin carbon films. *Science* **306**, 666–9, doi:10.1126/science.1102896 (2004).
9. Zhang, Y., Tan, Y. W., Stormer, H. L. & Kim, P. Experimental observation of the quantum Hall effect and Berry's phase in graphene. *Nature* **438**, 201–4, doi:10.1038/nature04235 (2005).
10. Tao, L. *et al*. Silicene field-effect transistors operating at room temperature. *Nat. Nanotech* **10**, 227–231, doi:10.1038/nnano.2014.325 (2015).
11. Dávila, M. E., Xian, L., Cahangirov, S., Rubio, A. & Lay, G. L. Germanene: a novel two-dimensional germanium allotrope akin to graphene and silicene. *New J. Phys.* **16**, 095002, doi:10.1088/1367-2630/16/9/095002 (2014).
12. Zhu, F. F. *et al*. Epitaxial growth of two-dimensional stanene. *Nat. Mater.* **14**, 1020–5, doi:10.1038/nmat4384 (2015).
13. Zhang, X. L., Liu, L. F. & Liu, W. M. Quantum anomalous Hall effect and tunable topological states in 3d transition metals doped silicene. *Sci. Rep.* **4**, 3801, doi:10.1038/srep03801 (2014).
14. Tahir, M. & Schwingenschlögl, U. Valley polarized quantum Hall effect and topological insulator phase transitions in silicene. *Sci. Rep.* **3**, 1075, doi:10.1038/srep01075 (2013).
15. Sun, Z. *et al*. Graphene mode-locked ultrafast laser. *ACS Nano* **4**, 803–810, doi:10.1021/nn901703e (2010).
16. Schwierz, F. Graphene transistors. *Nat. Nanotech.* **5**, 487–96, doi:10.1038/nnano.2010.89 (2010).
17. Akbari, E. *et al*. Silicene and graphene nano materials in gas sensing mechanism. *RSC Adv.* **6**, 81647–81653, doi:10.1039/C6RA16736E (2016).
18. Novoselov, K. S. *et al*. Two-dimensional gas of massless Dirac fermions in graphene. *Nature* **438**, 197–200, doi:10.1038/nature04233 (2005).
19. Murakami, M., Iijima, S. & Yoshimura, S. Morphology and structure of a one-dimensional graphite polymer, poly-peri-naphthalene. *J. Appl. Phys.* **60**, 3856–70, doi:10.1063/1.337556 (1986).
20. Zhang, M., Wu, D. H., Xu, C. L., Xu, Y. F. & Wang, W. K. Ribbon-like nanostructures transformed from carbon nanotubes at high temperature and pressure. *Nanostruct. Mater.* **10**, 1145–1152, doi:10.1016/S0965-9773(98)00151-2 (1998).
21. Shibayama, Y., Sato, H., Enoki, T. & Endo, M. Disordered magnetism at the metal-insulator threshold in nano-graphite-based carbon materials. *Phys. Rev. Lett.* **84**, 1744–7, doi:10.1103/PhysRevLett.84.1744 (2000).
22. Affoune, A. M. *et al*. Experimental evidence of a single nano-graphene. *Chem. Phys. Lett.* **348**, 17–20, doi:10.1016/S0009-2614(01)01066-1 (2001).
23. Vogt, P. *et al*. Silicene: compelling experimental evidence for graphenelike two-dimensional silicon. *Phys. Rev. Lett.* **108**, 155501, doi:10.1103/PhysRevLett.108.155501 (2012).
24. Aufray, B. *et al*. Graphene-like silicon nanoribbons on Ag (110): A possible formation of silicene. *Appl. Phy. Lett.* **96**, 183102, doi:10.1063/1.3419932 (2010).
25. Li, L. F. *et al*. Buckled Germanene Formation on Pt(111). *Adv. Mater.* **26**, 4820–4824, doi:10.1002/adma.v26.28 (2014).
26. Derivaz, M. *et al*. Continuous germanene layer on Al (111). *Nano Lett.* **15**, 2510–6, doi:10.1021/acs.nanolett.5b00085 (2015).
27. van den Broek, B. *et al*. Two-dimensional hexagonal tin: ab initio geometry, stability, electronic structure and functionalization. *2D Materials* **1**, 021004, doi:10.1088/2053-1583/1/2/021004 (2014).
28. Matthes, L., Pulci, O. & Bechstedt, F. Optical properties of two-dimensional honeycomb crystals graphene, silicene, germanene, and tinene from first principles. *New J. Phys.* **16**, 105007, doi:10.1088/1367-2630/16/10/105007 (2014).
29. Cai, B. *et al*. Tinene: a two-dimensional Dirac material with a 72 meV band gap. *Phys. Chem. Chem. Phys.* **17**, 12634–8, doi:10.1039/c5cp00563a (2015).
30. Liu, C. C., Jiang, H. & Yao, Y. Low-energy effective Hamiltonian involving spin-orbit coupling in silicene and two-dimensional germanium and tin. *Phys. Rev. B* **84**, 195430, doi:10.1103/PhysRevB.84.195430 (2011).
31. Chen, S. C., Wu, C. L., Wu, J. Y. & Lin, M. F. Magnetic quantization of sp^3 bonding in monolayer gray tin. *Phys. Rev. B* **94**, 045410, doi:10.1103/PhysRevB.94.045410 (2016).
32. Matthes, L., Pulci, O. & Bechstedt, F. Massive Dirac quasiparticles in the optical absorbance of graphene, silicene, germanene, and tinene. *J. Phys.: Condens. Matter* **25**, 395305, doi:10.1088/0953-8984/25/39/395305 (2013).
33. Tabert, C. J. & Nicol, E. J. Magneto-optical conductivity of silicene and other buckled honeycomb lattices. *Phys. Rev. B* **88**, 085434, doi:10.1103/PhysRevB.88.085434 (2013).
34. Lai, Y. H., Ho, J. H., Chang, C. P. & Lin, M. F. Magnetoelectronic properties of bilayer Bernal graphene. *Phys. Rev. B* **77**, 085426, doi:10.1103/PhysRevB.77.085426 (2008).

35. Lin, C. Y., Wu, J. Y., Ou, Y. J., Chiu, Y. H. & Lin, M. F. Magneto-electronic properties of multilayer graphenes. *Phys. Chem. Chem. Phys.* **17**, 26008–35, doi:10.1039/c5cp05013h (2015).
36. Lu, C. L., Chang, C. P., Huang, Y. C., Chen, R. B. & Lin, M. F. Influence of an electric field on the optical properties of few-layer graphene with AB stacking. *Phys. Rev. B* **73**, 144427, doi:10.1103/PhysRevB.73.144427 (2006).
37. Lin, M. F. & Shung, K. W.-K. Plasmons and optical-properties of carbon nanotubes. *Phys. Rev. B* **50**, Rapid Commun., 17744–17747, doi:10.1103/PhysRevB.50.17744 (1994).
38. Reining, L., Olevano, V., Rubio, A. & Onida, G. Excitonic effects in solids described by time-dependent density-functional theory. *Phys. Rev. Lett.* **88**, 066404, doi:10.1103/PhysRevLett.88.066404 (2002).
39. Slater, J. C. & Koster, G. F. Simplified LCAO method for the periodic potential problem. *Phys. Rev* **94**, 1498–1524, doi:10.1103/PhysRev.94.1498 (1954).
40. Ohta, T., Bostwick, A., Seyller, T., Horn, K. & Rotenberg, E. Controlling the electronic structure of bilayer graphene. *Science* **313**, 951–954, doi:10.1126/science.1130681 (2006).
41. Siegel, D. A., Regan, W., Fedorov, A. V., Zettl, A. & Lanzara, A. Charge-carrier screening in single-layer graphene. *Phys. Rev. Lett.* **110**, 146802, doi:10.1103/PhysRevLett.110.146802 (2013).
42. Kim, K. S. *et al.* Coexisting massive and massless Dirac fermions in symmetry-broken bilayer graphene. *Nat. Mater.* **12**, 887–892, doi:10.1038/nmat3717 (2013).
43. Ohta, T. *et al.* Interlayer interaction and electronic screening in multilayer graphene investigated with angle-resolved photoemission spectroscopy. *Phys. Rev. Lett.* **98**, 206802, doi:10.1103/PhysRevLett.98.206802 (2007).
44. Lauffer, P. *et al.* Atomic and electronic structure of few-layer graphene on SiC (0001) studied with scanning tunneling microscopy and spectroscopy. *Phys. Rev. B* **77**, 155426, doi:10.1103/PhysRevB.77.155426 (2008).
45. Pierucci, D. *et al.* Evidence for flat bands near the Fermi level in epitaxial rhombohedral multilayer graphene. *ACS Nano* **9**, 5432–5439, doi:10.1021/acsnano.5b01239 (2015).
46. Yankowitz, M., Wang, F., Lau, C. N. & LeRoy, B. J. Local spectroscopy of the electrically tunable band gap in trilayer graphene. *Phys. Rev. B* **87**, 165102, doi:10.1103/PhysRevB.87.165102 (2013).
47. Li, G., Luican, A. & Andrei, E. Y. Scanning tunneling spectroscopy of graphene on graphite. *Phys. Rev. Lett.* **102**, 176804, doi:10.1103/PhysRevLett.102.176804 (2009).
48. Tapaszto, L., Dobrik, G., Lambin, P. & Biro, L. P. Tailoring the atomic structure of graphene nanoribbons by scanning tunnelling microscope lithography. *Nat. Nanotech.* **3**, 397–401, doi:10.1038/nnano.2008.149 (2008).
49. Tao, C. *et al.* Spatially resolving edge states of chiral graphene nanoribbons. *Nat. Phys* **7**, 616–620, doi:10.1038/nphys1991 (2011).
50. Wilder, J. W., Venema, L. C., Rinzler, A. G., Smalley, R. E. & Dekker, C. Electronic structure of atomically resolved carbon nanotubes. *Nature* **391**, 59–62, doi:10.1038/34139 (1998).
51. Odom, T. W., Huang, J. L., Kim, P. & Lieber, C. M. Atomic structure and electronic properties of single-walled carbon nanotubes. *Nature* **391**, 62–64, doi:10.1038/34145 (1998).
52. Odom, T. W., Huang, J. L. & Lieber, C. M. STM studies of single-walled carbon nanotubes. *J. Phys.: Condensed Matter* **14**, R145 (2002).
53. Li, Z. Q. *et al.* Band structure asymmetry of bilayer graphene revealed by infrared spectroscopy. *Phy. Rev. Lett.* **102**, 037403, doi:10.1103/PhysRevLett.102.037403 (2009).
54. Zhang, L. M. *et al.* Determination of the electronic structure of bilayer graphene from infrared spectroscopy. *Phys. Rev. B* **78**, 235408, doi:10.1103/PhysRevB.78.235408 (2008).
55. Mak, K. F., Lui, C. H., Shan, J. & Heinz, T. F. Observation of an electric-field-induced band gap in bilayer graphene by infrared spectroscopy. *Phys. Rev. Lett.* **102**, 256405, doi:10.1103/PhysRevLett.102.256405 (2009).
56. Zhang, Y. *et al.* Direct observation of a widely tunable bandgap in bilayer graphene. *Nature* **459**, 820–823, doi:10.1038/nature08105 (2009).
57. Lui, C. H., Li, Z., Mak, K. F., Cappelluti, E. & Heinz, T. F. Observation of an electrically tunable band gap in trilayer graphene. *Nat. Phys.* **7**, 944–947, doi:10.1103/PhysRevLett.108.156801 (2011).
58. Liu, K. *et al.* Systematic determination of absolute absorption cross-section of individual carbon nanotubes. *Proceedings of the National Academy of Sciences* **111**, 7564–7569, doi:10.1073/pnas.1318851111 (2014).
59. Blancon, J. C. *et al.* Direct measurement of the absolute absorption spectrum of individual semiconducting single-wall carbon nanotubes. *Nat. commun.* **4**, 2542, doi:10.1038/ncomms3542 (2013).

Acknowledgements

This work was supported by the MOST of Taiwan, under Grant Nos MOST 105-2112-M-006-007-MY3 and MOST 104-2112-M-017-001.

Author Contributions

M.F.L. conceived this study. R.B.C. performed the major part of the calculations and the theoretical derivations. R.B.C. and M.F.L. composed the manuscript. S.C.C. and C.W.C. gave very useful suggestions for this research. All authors discussed the results and approved the final manuscript.

Additional Information

Competing Interests: The authors declare that they have no competing interests.

Publisher's note: Springer Nature remains neutral with regard to jurisdictional claims in published maps and institutional affiliations.